Advances in Applied Mathematics and Mechanics
Adv. Appl. Math. Mech., Vol. **8**, No. 5, pp. 703-721

DOI: 10.4208/aamm.2015.m1071
October 2016

A Switch Function-Based Gas-Kinetic Scheme for Simulation of Inviscid and Viscous Compressible Flows

Yu Sun[1], Chang Shu[1,*], Liming Yang[2] and C. J. Teo[1]

[1] *Department of Mechanical Engineering, National University of Singapore 10 Kent Ridge Crescent, Singapore 119260, Singapore*
[2] *Department of Aerodynamics, College of Aerospace Engineering, Nanjing University of Aeronautics and Astronautics, Yudao Street, Nanjing 210016, China*

Received 8 May 2015; Accepted (in revised version) 2 July 2015

Abstract. In this paper, a switch function-based gas-kinetic scheme (SF-GKS) is presented for the simulation of inviscid and viscous compressible flows. With the finite volume discretization, Euler and Navier-Stokes equations are solved and the SF-GKS is applied to evaluate the inviscid flux at cell interface. The viscous flux is obtained by the conventional smooth function approximation. Unlike the traditional gas-kinetic scheme in the calculation of inviscid flux such as Kinetic Flux Vector Splitting (KFVS), the numerical dissipation is controlled with a switch function in the present scheme. That is, the numerical dissipation is only introduced in the region around strong shock waves. As a consequence, the present SF-GKS can well capture strong shock waves and thin boundary layers simultaneously. The present SF-GKS is firstly validated by its application to the inviscid flow problems, including 1-D Euler shock tube, regular shock reflection and double Mach reflection. Then, SF-GKS is extended to solve viscous transonic and hypersonic flow problems. Good agreement between the present results and those in the literature verifies the accuracy and robustness of SF-GKS.

AMS subject classifications: 20B40

Key words: Switch function, gas-kinetic scheme, numerical dissipation, inviscid and viscous flows.

1 Introduction

In the last few decades, the gas-kinetic scheme has been developed systematically and applied in a wide range of flow problems. This approach enjoys a number of advantages, such as robustness, positivity-preserving and satisfying the entropy condition. In

*Corresponding author.
Email: mpeshuc@nus.edu.sg (C. Shu)

 ©2016 Global Science Press

https://doi.org/10.4208/aamm.2015.m1071 Published online by Cambridge University Press

addition, the "carbuncle phenomenon" can also be avoided in the hypersonic flow simulation, which is quite attractive as compared with conventional Riemann solvers. The gas-kinetic scheme is based on the Boltzmann equation, in which a single gas distribution function is used to describe the entire fluid state. However, due to high dimensionality and complicated collision term, it seems impractical to solve the Boltzmann equation directly except for the simplest problem [1]. On the other hand, the Euler and Navier-Stokes equations are accurate enough in the continuum regime. In fact, the Euler and Navier-Stokes equations can be derived from Boltzmann equation with the Chapman-Enskog expansion analysis. It may be a good choice to combine the Euler/Navier-Stokes solver with the gas-kinetic scheme. That is, with the finite volume discretization, the Euler and Navier-Stokes equations are solved at cell centers and the gas-kinetic scheme is applied to evaluate the numerical flux at cell interfaces.

An early example of gas-kinetic scheme can be referred to the equilibrium flux method (EFM), which was proposed by Pullin [2] for inviscid flows. Mandal and Deshpande [3] pioneered the work of kinetic flux-vector splitting (KFVS) to solve the Euler equations. Furthermore, Chou and Baganoff [4] extended the KFVS scheme for the Navier-Stokes equations. The KFVS has been demonstrated with good positivity property for simulation of flows with strong shock waves [5]. However, as these methods are based on collisionless Boltzmann equation, they usually produce a large numerical viscosity and heat conduction because the numerical dissipation of KFVS is proportional to the mesh size [6]. As a way to reduce the numerical dissipation, Xu [7] proposed the Totally Thermalized Transport (TTT) scheme, where particle collisions are introduced instantaneously in the evaluation of numerical flux at cell interface. The TTT scheme can resolve a boundary layer accurately, but it suffers from oscillations in the region of discontinuity due to insufficient numerical dissipation. It seems that all the above methods cannot capture both the strong shock wave and thin boundary layer at the same time. One of the significant developments in gas-kinetic schemes is the gas-kinetic BGK scheme, which was proposed by Prendergast and Xu [8], Chae et al. [9], Xu [10] and other researchers. In the gas-kinetic BGK scheme, the particle collision effect is taken into consideration in the gas evolution stage and a BGK collision model [11] is applied in the flux evaluation. As a consequence, the dissipation is controlled by the real collision time rather than by the time step. In contrast to conventional upwind schemes, the gas-kinetic BGK scheme computes the inviscid and viscous fluxes simultaneously from the solution of Boltzmann equation with collision term. Numerical results show that this scheme can provide accurate and stable solutions for both inviscid and viscous flow problems [12–20]. However, the gas-kinetic BGK scheme is not completely free from drawbacks. It is usually more complicated and inefficient than conventional CFD schemes. The wish to develop a simple and efficient gas-kinetic scheme to capture both the strong shock wave and thin boundary layer simultaneously motivates the present work.

In the gas-kinetic scheme, the gas distribution function can be expressed as $f = f^{eq} + f^{neq}$, where f^{eq} is the equilibrium distribution function and f^{neq} is the non-equilibrium distribution function. According to Chapman-Enskog analysis, it is known that the equi-

https://doi.org/10.4208/aamm.2015.m1071 Published online by Cambridge University Press

librium part f^{eq} contributes to the inviscid flux and the non-equilibrium part f^{neq} contributes to the viscous flux. As a result, for the evaluation of inviscid flux, only the equilibrium distribution function is needed. This kind of method can resolve a boundary layer accurately, but it will become unstable in the region of discontinuity, such as around the shock wave. Therefore, the non-equilibrium part of distribution function should be added to introduce numerical dissipation, which is very helpful to capture the strong shock wave. One of the examples is the KFVS scheme. However, owing to the large numerical dissipation introduced in the KFVS scheme, the results might be polluted in the smooth region. From this process, it can be concluded that the numerical dissipation should only be introduced in the region around strong shock waves to get a stable and accurate solution. In this work, the numerical dissipation is controlled by a switch function. That is, in the smooth region such as in the boundary layer, the switch function approaches to zero, implying that a little numerical dissipation is introduced. On the other hand, in the region of discontinuity such as strong shock waves, it tends to one, indicating that a large numerical dissipation is introduced. The above feature shows the major advantage of the present switch function-based gas-kinetic scheme (SF-GKS) as the strong shock wave and thin boundary layer can be well captured simultaneously with the introduction of the switch function. Another advantage is that the value of switch function can be easily determined, which makes this method efficient and easy to be implemented. To validate the present scheme, some inviscid flows such as 1-D Euler shock tube, regular shock reflection and double Mach reflection are simulated first. Then, the scheme is extended to simulate viscous flows. To solve Navier-Stokes equations, the inviscid flux is calculated by the SF-GKS and the viscous flux is computed by the smooth function approximation. The viscous flow problems such as compressible turbulent flows around RAE2822 airfoil and hypersonic flows over a half cylinder are simulated. Numerical results show that the SF-GKS can well capture both the thin boundary layer and strong shock wave.

2 Methodology

2.1 Governing equations discretized by finite volume method

For an inviscid flow, Euler equations are commonly used in conventional computational fluid dynamics. On the other hand, Navier-Stokes equations are usually used to simulate viscous flows. Generally, with the finite volume discretization, the discretized form of 2-D Navier-Stokes equations can be written as

$$\frac{d\mathbf{W}}{dt}+\frac{1}{\Omega}\sum_{i=1}^{N}(\mathbf{F}_c-\mathbf{F}_v)_i S_i=0, \tag{2.1}$$

where, Ω and N are the volume and number of interfaces of the control volume and S_i is the length of interface i. The conservative variables $\mathbf{W}$, convective flux $\mathbf{F}_c$ and viscous

https://doi.org/10.4208/aamm.2015.m1071 Published online by Cambridge University Press

flux $\mathbf{F}_v$ are given by

$$\mathbf{W}=\begin{bmatrix}\rho\\ \rho U\\ \rho V\\ \rho E\end{bmatrix},\quad \mathbf{F}_c=\begin{bmatrix}\rho U_n\\ \rho U U_n+n_x p\\ \rho V U_n+n_y p\\ (\rho E+p)U_n\end{bmatrix},\quad \mathbf{F}_v=\begin{bmatrix}0\\ n_x\tau_{xx}+n_y\tau_{xy}\\ n_x\tau_{yx}+n_y\tau_{yy}\\ n_x\Theta_x+n_y\Theta_y\end{bmatrix}. \tag{2.2}$$

In the above equation, ρ, U, V and p are the density, velocities and pressure of the mean flow. E is the total energy defined as

$$E=\frac{p}{(\gamma-1)\rho}+\frac{1}{2}(U^2+V^2), \tag{2.3}$$

where γ is the specific heat ratio. (n_x,n_y) is the unit normal vector of the control surface and U_n is the normal velocity of the cell interface. In the viscous flux $\mathbf{F}_v$, τ_{ij} denotes the components of viscous stress tensor and Θ_i is energy flux contributed by the viscous stress and the heat transfer. The formulations and detailed implementation of τ_{ij} and Θ_i will be introduced in Subsection 2.3.

As shown in Eq. (2.1), with the conservative variables at cell center, we need to evaluate numerical fluxes at cell interfaces. For inviscid flow problems, the viscous flux $\mathbf{F}_v$ is abandoned and only the inviscid flux $\mathbf{F}_c$ is to be evaluated. Therefore, the governing equations become the Euler equations

$$\frac{d\mathbf{W}}{dt}+\frac{1}{\Omega}\sum_{i=1}^{N}(\mathbf{F}_c)_i S_i=0. \tag{2.4}$$

While for the viscous flow problem, the viscous flux $\mathbf{F}_v$ is usually approximated by a smooth function, such as polynomial approximation. Therefore, for both inviscid and viscous flows, the remaining problem is the evaluation of inviscid flux $\mathbf{F}_c$ at cell interface, which is computed by the gas-kinetic scheme in this work. As shown in Fig. 1, the relationship between velocities in the normal and tangential directions (U_n,U_τ) and velocities in the Cartesian coordinate system (U,V) are

$$U_n=U\cdot n_x+V\cdot n_y,\quad U_\tau=V\cdot n_x-U\cdot n_y. \tag{2.5}$$

In the application of gas-kinetic scheme, the flux $\mathbf{F}_c$ at cell interface is calculated by the local application of Boltzmann equation, which can be expressed as [17]

$$\mathbf{F}_c=\int u_n\varphi_\alpha f\,d\Xi, \tag{2.6}$$

where u_n is the phase velocity in the normal direction of the interface, f is the particle distribution function, $d\Xi=dudvd\xi$ is the volume element in the phase space, φ_α is the moment given as

$$\varphi_\alpha=\left(1,\,u,\,v,\,\frac{1}{2}(u^2+v^2+\xi^2)\right)^T, \tag{2.7}$$

https://doi.org/10.4208/aamm.2015.m1071 Published online by Cambridge University Press

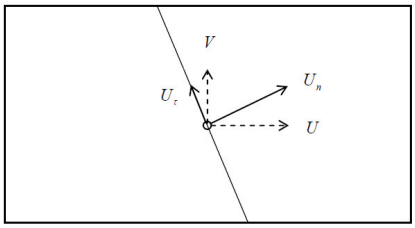


Figure 1: Schematic of velocity transformation at cell interface.

in which (u,v) are the phase velocities of particle in the Cartesian coordinate system and ξ is the internal energy.

Similar to Eq. (2.5), the relationship between the phase velocities in the normal and tangential directions (u_n,u_τ) and the phase velocities in the Cartesian coordinate system (u,v) are

$$u_n = u\cdot n_x + v\cdot n_y, \quad u_\tau = v\cdot n_x - u\cdot n_y, \tag{2.8}$$

and

$$u = u_n\cdot n_x - u_\tau\cdot n_y, \quad v = u_\tau\cdot n_x + u_n\cdot n_y. \tag{2.9}$$

Substituting Eq. (2.9) into Eq. (2.7), we have

$$\varphi_\alpha = \left(1, u_n\cdot n_x - u_\tau\cdot n_y, u_\tau\cdot n_x + u_n\cdot n_y, \frac{1}{2}(u_n^2+u_\tau^2+\xi^2)\right)^T. \tag{2.10}$$

With the definition of a new moment

$$\varphi_\alpha^* = \left(1, u_n, u_\tau, \frac{1}{2}(u_n^2+u_\tau^2+\xi^2)\right)^T \tag{2.11}$$

and its corresponding convective flux vector

$$\mathbf{F}_c^* = \int u_n\varphi_\alpha^* f d\Xi = (F_1^*, F_2^*, F_3^*, F_4^*)^T, \tag{2.12}$$

the real convective flux vector $\mathbf{F}_c$ can be obtained by substituting Eq. (2.10) into Eq. (2.6) and using Eq. (2.12)

$$\mathbf{F}_c = \int u_n\varphi_\alpha f d\Xi = (F_1^*,\ F_2^*n_x - F_3^*n_y,\ F_3^*n_x + F_2^*n_y,\ F_4^*)^T. \tag{2.13}$$

From Eq. (2.13), it is clear that the calculation of $\mathbf{F}_c$ is equivalent to the evaluation of $\mathbf{F}_c^*$ and the key issue is to obtain the gas distribution function f. In the next part, a switch function-based gas-kinetic scheme (SF-GKS) will be introduced to evaluate the gas distribution function f, which can capture both strong shock waves and thin boundary layers.

https://doi.org/10.4208/aamm.2015.m1071 Published online by Cambridge University Press

2.2 Evaluation of inviscid flux by switch function-based gas-kinetic scheme

2.2.1 Boltzmann equation and 5 conservation forms of moments to recover Euler equations

Without the external forcing term, The Boltzmann equation with Bhatnagar-Gross-Krook (BGK) model can be written as

$$\frac{\partial f}{\partial t}+u\frac{\partial f}{\partial x}+v\frac{\partial f}{\partial y}=-\frac{f-g}{\tau}, \tag{2.14}$$

where f is the particle distribution function and g is the equilibrium particle distribution function. τ is the collision time, which is determined by dynamic viscosity and pressure. The right side of the equation is the collision term which alters the distribution function from f to g within a collision time scale τ. Both f and g are functions of space (x,y), time (t), particle velocity (u,v) and internal energy ξ. The internal degree of freedom K in ξ is determined by the space dimension and the specific heat ratio with the relation $K+D=2/(\gamma-1)$, where D is the abbreviation of the dimension. The equilibrium state g of Maxwellian distribution function is

$$g=\rho\left(\frac{\lambda}{\pi}\right)^{\frac{K+2}{2}}e^{-\lambda((u-U)^2+(v-V)^2+\xi^2)}. \tag{2.15}$$

Here $\lambda=m/2kT=1/2RT$, where m is the molecular mass, k is the Boltzmann constant, R is the gas constant and T is the temperature. In the equilibrium state, the internal energy is $\xi^2=\xi_1^2+\xi_2^2+\cdots+\xi_K^2$.

With the above Maxwellian distribution function, to recover Euler equations by Eq. (2.14) through Chapman-Enskog expansion analysis, the following 5 conservation forms of moments should be satisfied,

$$\int g d\Xi=\rho, \tag{2.16a}$$

$$\int g u_\alpha d\Xi=\rho U_\alpha, \tag{2.16b}$$

$$\int g\left(u_\alpha u_\alpha+\sum_{j=1}^{K}\xi_j^2\right)d\Xi=\rho(U_\alpha U_\alpha+bRT), \tag{2.16c}$$

$$\int g u_\alpha u_\beta d\Xi=\rho U_\alpha U_\beta+p\delta_{\alpha\beta}, \tag{2.16d}$$

$$\int g\left(u_\alpha u_\alpha+\sum_{j=1}^{K}\xi_j^2\right)u_\beta d\Xi=\rho\left[U_\alpha U_\alpha+(b+2)RT\right]U_\beta, \tag{2.16e}$$

where u_α, u_β and U_α, U_β are the phase velocity and macroscopic flow velocity in α and β direction. $b=K+D$ represents the total degree of freedom of molecules. $d\Xi=du_\alpha du_\beta d\xi_1 d\xi_2\cdots d\xi_K$ is the volume element in the phase space. The integral domains in

https://doi.org/10.4208/aamm.2015.m1071 Published online by Cambridge University Press

all the above equations are from $-\infty$ to $+\infty$. In the above 5 equations, Eqs. (2.16a)-(2.16c) are applied to recover fluid density, momentum and energy, respectively. On the other hand, Eqs. (2.16d) and (2.16e) are to recover the convective flux of momentum equations and energy equation.

2.2.2 A switch function-based gas-kinetic scheme

In the above subsection, 5 conservation forms to recover the Euler equations are presented in the Cartesian coordinate system. As the convective flux is evaluated at the local interface, a local coordinate system is used in the following derivation of distribution function f. With Chapman-Enskog analysis, the non-equilibrium distribution function can be approximated as

$$f^{neq} = -\tau\left(\frac{\partial}{\partial t} + \mathbf{u}\cdot\nabla\right) f^{eq}, \tag{2.17}$$

where the equilibrium distribution function is

$$f^{eq} = g. \tag{2.18}$$

Therefore, the real distribution function in the local Boltzmann equation becomes

$$f = f^{eq} + f^{neq} = g - \tau\left(\frac{\partial g}{\partial t} + u_n\frac{\partial g}{\partial n} + u_\tau\frac{\partial g}{\partial \tau}\right). \tag{2.19}$$

By applying the Taylor series expansion in time and physical space, the above equation can be simplified to

$$f(0,0,t+\delta t) = g(0,0,t+\delta t) - \frac{\tau}{\delta t}[g(0,0,t+\delta t) - g(-u_n\delta t, -u_\tau\delta t, t)], \tag{2.20}$$

where $f(0,0,t+\delta t)$ is the gas distribution function at the interface, and $g(0,0,t+\delta t)$ and $g(-u_n\delta t,-u_\tau\delta t,t)$ are the equilibrium distribution functions at cell interface and its surrounding points, respectively. δt is the streaming time step. Here, $\tau/\delta t$ can be viewed as the dimensionless collision time. For the evaluation of inviscid flux, $g(-u_n\delta t,-u_\tau\delta t,t)$ can be taken as a piecewise constant function around cell interface

$$g(-u_n\delta t,-u_\tau\delta t,t) = \begin{cases} g_l, & u_n > 0, \\ g_r, & u_n < 0, \end{cases} \tag{2.21}$$

where g_l and g_r stand for the equilibrium distribution functions at the left and right sides of cell interface, respectively.

According to the Chapman-Enskog analysis, the equilibrium part f^{eq} of the distribution function in Eq. (2.20) contributes to the inviscid flux. On the other hand, the non-equilibrium part f^{neq} contributes to the viscous flux. As the SF-GKS is merely used to evaluate the inviscid flux, only the equilibrium part is needed:

$$f(0,0,t+\delta t) = g(0,0,t+\delta t). \tag{2.22}$$

https://doi.org/10.4208/aamm.2015.m1071 Published online by Cambridge University Press

In Eq. (2.22), no numerical dissipation is introduced. Therefore, this scheme can capture the thin boundary layer accurately. However, in the region of discontinuity, such as around strong shock waves, this scheme will be unstable and sometimes diverge because of no numerical dissipation.

Another approach is to include the non-equilibrium part f^{neq} in the distribution function to introduce the numerical dissipation. By setting $\tau/\delta t=1$, Eq. (2.20) becomes

$$f(0,0,t+\delta t)=g(-u_n\delta t,-u_\tau\delta t,t). \tag{2.23}$$

In fact, Eq. (2.23) is based on the collisionless Boltzmann equation and the numerical dissipation is proportional to the mesh size [6]. It is known that a large numerical dissipation is introduced in this scheme. Therefore, Eq. (2.23) performs stably and can well simulate hypersonic inviscid flows. Nevertheless, owing to the large dissipation introduced, the results will easily get smeared in the smooth region, such as in thin boundary layers.

In the conventional gas-kinetic scheme [6], the distribution function is

$$\begin{aligned} f(0,0,t+\delta t)=&g(0,0,t+\delta t)-\eta[g(0,0,t+\delta t)-g(-u_n\delta t,-u_\tau\delta t,t)]\\ =&(1-\eta)\cdot g(0,0,t+\delta t)+\eta\cdot g(-u_n\delta t,-u_\tau\delta t,t), \end{aligned} \tag{2.24}$$

where η is a constant with $\eta\in[0,1]$. Obviously, Eq. (2.24) is exactly the same as Eq. (2.20) if we denote $\eta=\tau/\delta t$. In Eq. (2.24), the constant η controls the numerical dissipation. To be more specific, when $\eta=0$, Eq. (2.24) is the same as Eq. (2.22), in which there is no numerical dissipation. When $\eta=1$, the distribution function becomes Eq. (2.23), where a large numerical dissipation is introduced. In the practical application, η is usually taken as a constant in the whole domain, such as $\eta=0.5$. However, the introduction of constant η in Eq. (2.24) means that the numerical dissipation is added uniformly in the regions of strong shock waves and thin boundary layers, which is not reasonable. The above problem motivates the current work by introducing a switch function to control the numerical dissipation. To be specific, in the region of thin boundary layer, the numerical dissipation should not be introduced and η should be close to 0, while in the region of discontinuity, large dissipation should be introduced to ensure the stable solution with $\eta=1$. In order to distinguish it from the constant η, the switch function is denoted as η^+ with the definition of

$$\eta^+=\tanh\left(C\frac{|p_L-p_R|}{p_L+p_R}\right), \tag{2.25}$$

where $\tanh(x)$ is the hyperbolic tangent function; C is the amplification factor and $C=10$ is used in the present work; p_L and p_R are the pressure at the left and right side of cell interface. Therefore, the distribution function becomes

$$f(0,0,t+\delta t)=(1-\eta^+)\cdot g(0,0,t+\delta t)+\eta^+\cdot g(-u_n\delta t,-u_\tau\delta t,t). \tag{2.26}$$

From the characteristics of the hyperbolic tangent function, it can be seen that η^+ ranges from 0 to 1. In the smooth region, the switch function η^+ is close to 0 due to the small

https://doi.org/10.4208/aamm.2015.m1071 Published online by Cambridge University Press

pressure difference at two sides of cell interface and Eq. (2.26) approaches Eq. (2.22). In the region of discontinuity, there will be a large difference of pressure at the two sides of interface and Eq. (2.26) approaches Eq. (2.23).

From the above distribution function in Eq. (2.26), the numerical fluxes for the mass, momentum and energy across the cell interface can be calculated by

$$\begin{aligned}\mathbf{F}_c^* &= \int u_n \varphi_\alpha^* f d\Xi \\ &= (1-\eta^+)\cdot \int u_n \varphi_\alpha^* g(0,0,t+\delta t) d\Xi + \eta^+ \cdot \int u_n \varphi_\alpha^* g(-u_n\delta t,-u_\tau \delta t,t) d\Xi. \end{aligned} \tag{2.27}$$

In the above equation, the convective flux $\mathbf{F}_c^*$ can be separated into two parts: the flux contributed by $g(0,0,t+\delta t)$, which is denoted as $\mathbf{F}_{c,0}^*$ and the flux contributed by $g(-u_n\delta t,-u_\tau\delta t,t)$, which is denoted as $\mathbf{F}_{c,1}^*$. As a result, the total inviscid flux across cell interface can be written as

$$\mathbf{F}_c^* = (1-\eta^+)\cdot \mathbf{F}_{c,0}^* + \eta^+ \cdot \mathbf{F}_{c,1}^*. \tag{2.28}$$

In Eq. (2.1), the governing equations are solved by the finite volume method, and conservative flow variables are defined at cell centers. With the conservative variables at cell center, the conservative variables at the left and right sides of cell interface can be obtained by interpolation. Then, the velocities in the Cartesian coordinate system should be transferred to the velocities in the normal and tangential directions of the interface by Eq. (2.5). In order to evaluate the flux $\mathbf{F}_{c,0}^*$ contributed by $g(0,0,t+\delta t)$, the conservative variables at the cell interface should be computed at first. By applying the compatibility condition $\int (g-f)\varphi_\alpha^* d\Xi = 0$, the conservative variables at cell interface can be computed as

$$\mathbf{W}_0^* = \int \varphi_\alpha^* f(0,0,t+\delta t) d\Xi = \int \varphi_\alpha^* g(0,0,t+\delta t) d\Xi, \tag{2.29}$$

where $\mathbf{W}_0^*$ is the vector of conservative variables at cell interface.

By substituting Eq. (2.26) into Eq. (2.29), we have

$$\begin{aligned}\mathbf{W}_0^* &= \int \varphi_\alpha^* f(0,0,t+\delta t) d\Xi \\ &= \int \varphi_\alpha^* g(0,0,t+\delta t) d\Xi - \eta^+ \Big[\int \varphi_\alpha^* g(0,0,t+\delta t) d\Xi - \int \varphi_\alpha^* g(-u_n\delta t,-u_\tau\delta t,t) d\Xi \Big]. \end{aligned} \tag{2.30}$$

Using Eq. (2.29), we can find the relation in Eq. (2.30) that

$$\int \varphi_\alpha^* g(0,0,t+\delta t) d\Xi = \int \varphi_\alpha^* g(-u_n\delta t,-u_\tau\delta t,t) d\Xi. \tag{2.31}$$

By substituting Eq. (2.21) and Eq. (2.31) into Eq. (2.29), we have

$$\mathbf{W}_0^* = \int \varphi_\alpha^* g(-u_n\delta t,-u_\tau\delta t,t) d\Xi = \int\int_{u_n>0} \varphi_\alpha^* g_l d\Xi + \int\int_{u_n<0} \varphi_\alpha^* g_r d\Xi, \tag{2.32}$$

https://doi.org/10.4208/aamm.2015.m1071 Published online by Cambridge University Press

Eq. (2.32) shows that the conservative variables on the interface can be constructed by the flow variables at its left and right sides. In the above equation, the integral domains for normal velocity u_n and tangential velocity u_τ are different with the consideration of a discontinuity around the interface. In the tangential direction, the integral domain is always from $-\infty$ to $+\infty$. However, in the normal direction, the integral domain is from $-\infty$ to 0 on the right side and 0 to $+\infty$ on the left side. The explicit expressions of $\mathbf{W}_0^*$ can be given as

$$\rho = \rho_l \cdot a_l + \rho_r \cdot a_r, \tag{2.33a}$$
$$\rho U_n = \rho_l \cdot b_l + \rho_r \cdot b_r, \tag{2.33b}$$
$$\rho U_\tau = \rho_l U_{\tau,l} \cdot a_l + \rho_r U_{\tau,r} \cdot a_r, \tag{2.33c}$$
$$\rho E = \frac{1}{2}\rho_l[c_l + (U_{\tau,l}^2 + (b-1)RT_l)\cdot a_l] + \frac{1}{2}\rho_r[c_r + (U_{\tau,r}^2 + (b-1)RT_r)\cdot a_r], \tag{2.33d}$$

where

$$a_l = \frac{1}{2}erfc\left(-\sqrt{\lambda_l}U_{n,l}\right), \qquad a_r = \frac{1}{2}erfc\left(\sqrt{\lambda_r}U_{n,r}\right), \tag{2.34a}$$
$$b_l = U_{n,l}\cdot a_l + \frac{1}{2}\frac{e^{-\lambda_l {U_{n,l}}^2}}{\sqrt{\pi\lambda_l}}, \qquad b_r = U_{n,r}\cdot a_r - \frac{1}{2}\frac{e^{-\lambda_r {U_{n,r}}^2}}{\sqrt{\pi\lambda_r}}, \tag{2.34b}$$
$$c_l = U_{n,l}\cdot b_l + \frac{1}{2\lambda_l}\cdot a_l, \qquad c_r = U_{n,r}\cdot b_r + \frac{1}{2\lambda_r}\cdot a_r, \tag{2.34c}$$

and "$\cdot_l$" and "$\cdot_r$" ("$\cdot$" stands for any variable) denote the variable at the left and right side of interface, respectively.

Once $\mathbf{W}_0^*$ is obtained, the equilibrium distribution function $g(0,0,t+\delta t)$ can be constructed by Eq. (2.15) and correspondingly, the flux $\mathbf{F}_{c,0}^*$ can be evaluated as

$$\mathbf{F}_{c,0}^* = \int u_n \varphi_\alpha^* g(0,0,t+\delta t)d\Xi = \begin{bmatrix} \rho U_n \\ \rho U_n^2 + p \\ \rho U_n U_\tau \\ (\rho E + p)U_n \end{bmatrix}. \tag{2.35}$$

After the evaluation of flux $\mathbf{F}_{c,0}^*$, the flux $\mathbf{F}_{c,1}^*$ contributed by $g(-u_n\delta t, -u_\tau\delta t, t)$ is calculated as

$$\mathbf{F}_{c,1}^* = \int u_n \varphi_\alpha^* g(-u_n\delta t, -u_\tau\delta t, t)d\Xi = \int\int_{u_n>0} u_n \varphi_\alpha^* g_l d\Xi + \int\int_{u_n<0} u_n \varphi_\alpha^* g_r d\Xi. \tag{2.36}$$

Similarly, the explicit formulations of $\mathbf{F}_{c,1}^*$ can also be given as

$$F_{c,1}^*(1) = \rho_l \cdot b_l + \rho_r \cdot b_r, \tag{2.37a}$$
$$F_{c,1}^*(2) = \rho_l \cdot c_l + \rho_r \cdot c_r, \tag{2.37b}$$
$$F_{c,1}^*(3) = \rho_l U_{\tau,l} \cdot b_l + \rho_r U_{\tau,r} \cdot b_r, \tag{2.37c}$$
$$F_{c,1}^*(4) = \frac{1}{2}\rho_l[d_l + (U_{\tau,l}^2 + (b-1)RT_l)\cdot b_l] + \frac{1}{2}\rho_r[d_r + (U_{\tau,r}^2 + (b-1)RT_r)\cdot b_r], \tag{2.37d}$$

https://doi.org/10.4208/aamm.2015.m1071 Published online by Cambridge University Press

where a_l, a_r, b_l, b_r, c_l, c_r have been defined in Eqs. (2.34a)-(2.34c) and d_l, d_r are

$$d_l = U_{n,l}\cdot c_l + \frac{1}{\lambda_l}\cdot b_l, \quad d_r = U_{n,r}\cdot c_r + \frac{1}{\lambda_r}\cdot b_r. \tag{2.38}$$

Note that in the expressions (2.37a)-(2.37d), $F^*_{c,1}(m)$ means the mth component of the vector $\mathbf{F}^*_{c,1}$.

2.3 Evaluation of viscous flux by smooth function approximation

The convective flux $\mathbf{F_c}$ in Eq. (2.1) has been obtained by the above switch function-based gas-kinetic scheme and the Euler equations can be solved correspondingly. Nevertheless, when solving the viscous flow problem, the evaluation of viscous flux is also necessary. As has been presented in Eq. (2.2), the viscous flux can be written as

$$\mathbf{F}_v = \begin{bmatrix} 0 \\ n_x\tau_{xx} + n_y\tau_{xy} \\ n_x\tau_{yx} + n_y\tau_{yy} \\ n_x\left(u\tau_{xx} + v\tau_{xy} + \kappa\dfrac{\partial T}{\partial x}\right) + n_y\left(u\tau_{yx} + v\tau_{yy} + \kappa\dfrac{\partial T}{\partial y}\right) \end{bmatrix}. \tag{2.39}$$

Here, τ_{ij} is the stress

$$\tau_{ij} = \mu\left(\frac{\partial u_i}{\partial x_j} + \frac{\partial u_j}{\partial x_i} - \frac{2}{3}\frac{\partial u_k}{\partial x_k}\delta_{ij}\right)$$

and μ is the dynamic viscosity. $\kappa = \mu c_p/\mathrm{Pr}Re$ is the thermal conductivity, where c_p is the heat capacity, Pr and Re are the Prandtl and Reynolds numbers.

Owing to the elliptic nature of the viscous flux, the viscous flux $\mathbf{F}_v$ can be approximated by a smooth function. In FVM, the derivatives $\nabla\phi$ (ϕ stands for u, v and T) at the cell interface $(i+1/2,j)$ can be approximated by the finite volume method with application of Gauss theorem

$$\nabla\phi_{i+1/2,j} \approx \frac{1}{\Omega_{i+1/2,j}}\oint_{\partial\Omega_{i+1/2,j}} \phi\mathbf{n}ds. \tag{2.40}$$

As all the flow variables are defined at the cell center, a simple interpolation can be made to obtain the values of flow variables at nodes and cell interface in the evaluation of viscous flux.

3 Numerical examples

To validate the proposed switch function-based gas-kinetic scheme (SF-GKS), several numerical cases are considered. At first, the inviscid compressible flows are tested, including 1-D Euler shock tube, regular shock reflection and double Mach reflection. Furthermore, the SF-GKS is extended to solve viscous compressible flow problems, such as the

https://doi.org/10.4208/aamm.2015.m1071 Published online by Cambridge University Press

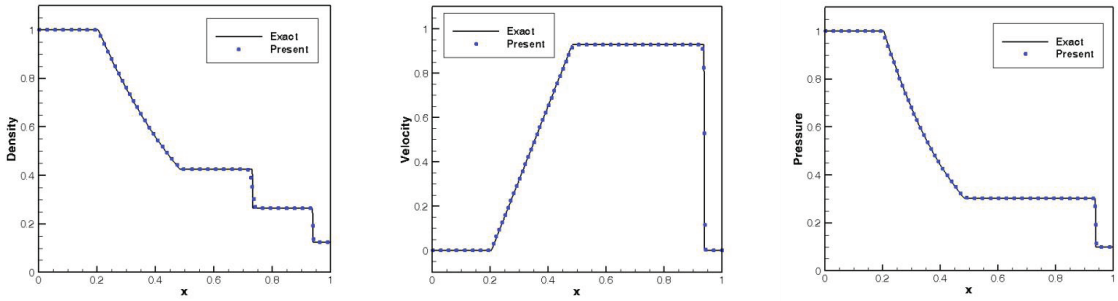
turbulent flow around RAE2822 airfoil and hypersonic flow around a half of cylinder. In the reconstruction stage to calculate the conservative variables at the two sides of cell interface, the Van Leer limiter [21] and the Venkatakrishnan's limiter [22] are adopted in the inviscid and viscous test cases, respectively.

1-D Euler shock tube

The one dimensional Euler shock tube is a standard Riemann problem. In the tube, there are two different initial constant states in the left and right parts. Three waves emerge from the initial discontinuity, which are rarefaction wave, contact discontinuity and shock wave. Two different Riemann problems are selected to test the performance of current SF-GKS. The initial conditions of first test case are

$$\rho_L=1.0, \qquad u_L=0.0, \qquad p_L=1.0,$$
$$\rho_R=0.125, \qquad u_R=0.0, \qquad p_R=0.1.$$

This is a mild test and the solution consists of a left rarefaction, a contact discontinuity and a right shock wave [23]. Fig. 2 shows the solution profiles at time $t=0.25$, in which the results of density, velocity and pressure are presented and well compared with exact solutions.



(a) (b) (c)

Figure 2: Comparison of density, velocity and pressure with the exact solution at time $t=0.25$ of Test Case 1.

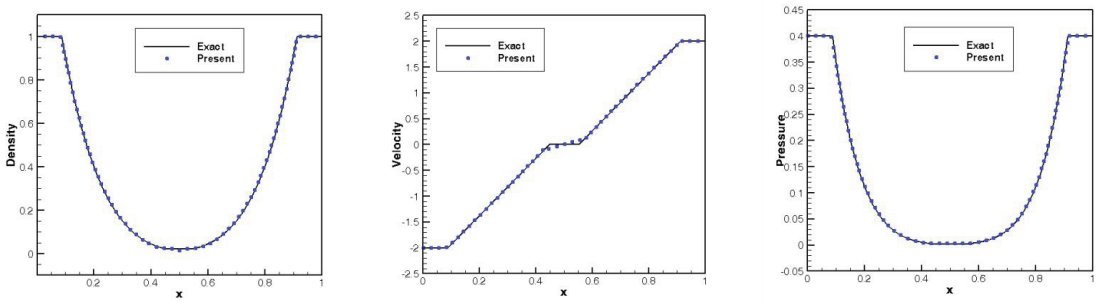
The other test is

$$\rho_L=1.0, \qquad u_L=-2.0, \qquad p_L=0.4,$$
$$\rho_R=1.0, \qquad u_R=2.0, \qquad p_R=0.4.$$

The solution from the above initial condition consists of two strong rarefactions and a trivial stationary contact discontinuity [23]. Therefore, this test case can be used to access the performance of this solver in the low density problem. Similar to the first test case, the results of density, velocity and pressure at time $t=0.15$ are shown in Fig. 3. The exact solution is also included for comparison.

From the above two tests, the results of SF-GKS match well with the the exact solutions and show stable performance for the one dimensional shock tube problem.

https://doi.org/10.4208/aamm.2015.m1071 Published online by Cambridge University Press



(a) (b) (c)

Figure 3: Comparison of density, velocity and pressure with the exact solution at time $t=0.15$ of Test Case 2.

Case 2: Regular shock reflection

To further validate the present scheme, the 2D regular shock reflection is tested. The compuational domain is a rectangle of length 4 and height 1. A uniform mesh of 120×40 is used. The Dirichlet conditions are imposed on the left and top boundaries, which are

$$\rho_L=1.0, \quad u_L=2.9, \quad v_L=0.0, \quad p_L=1/1.4,$$
$$\rho_T=1.69997, \quad u_T=2.61934, \quad v_T=-0.50633, \quad p_T=1.52819.$$

The right boundary condition is supersonic outflow where extrapolation is applied. A reflecting condition is applied along the bottom boundary. Fig. 4 shows the pressure contour in which the shock wave is captured well. Fig. 5 presents the density profile at the position of $y=0.5$. The exact solution [24] and the result obtained by Kinetic Flux Vector Splitting (KFVS) are also included for comparison and good agreeement can be found in these results. Furthermore, it can be seen that the present result is slightly better than KFVS results because of less numerical dissipation introduced.

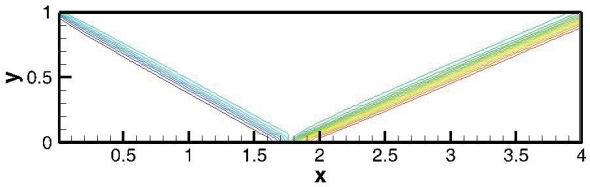


Figure 4: Pressure contour of the shock reflection.

Case 3: Double Mach reflection

The test case of double Mach reflection is a hypersonic flow problem with a pressure ratio of 116.5. Initially, a strong normal shock wave with Mach number 10 passes through a 30° wedge. The computational domain is chosen to be a rectangle of 4×1 with a uniform mesh of 480×120. The detailed information about the boundary conditions of this test can be found in [25]. Fig. 6 and Fig. 7 show the density and pressure contours at $t=0.2$

https://doi.org/10.4208/aamm.2015.m1071 Published online by Cambridge University Press

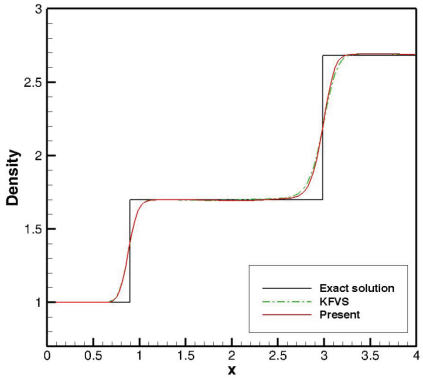
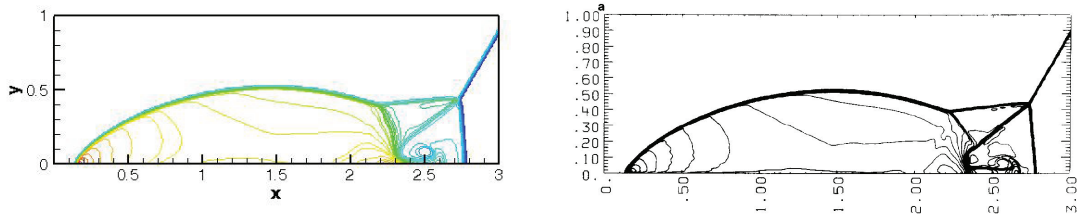


Figure 5: Comparison of density profile for the shock reflection along the line $y=0.5$.

by the present scheme. The complex flow structures such as the main shock, the oblique wave and the three-shock intersection are all well captured. As seen from the figures, the present results are in good agreement with those of Woodward and Colella [25].

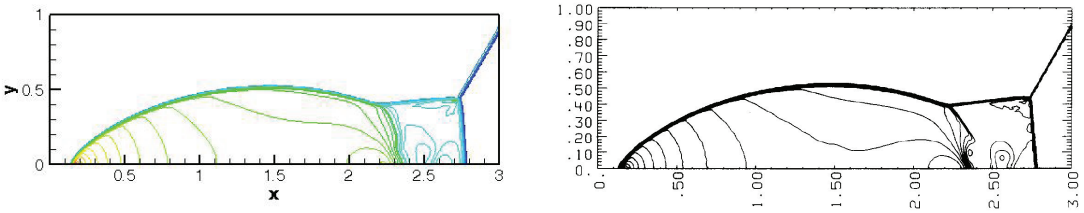
Case 4: Compressible turbulent flow around RAE2822 airfoil

The above 3 test cases are all inviscid flow problems and only the convective flux is evaluated. This test case is the transonic flow around RAE2822 airfoil and the viscous flux should also be calculated via the smooth function approximation. For this case, the free-stream conditions are set according to the experimental Case 9 in [26], with Mach number $M_\infty=0.73$, Reynolds number $Re=6.5\times10^6$ and the angle of attack $\alpha=2.79^\circ$. A 369×65 C-



(a) (b)

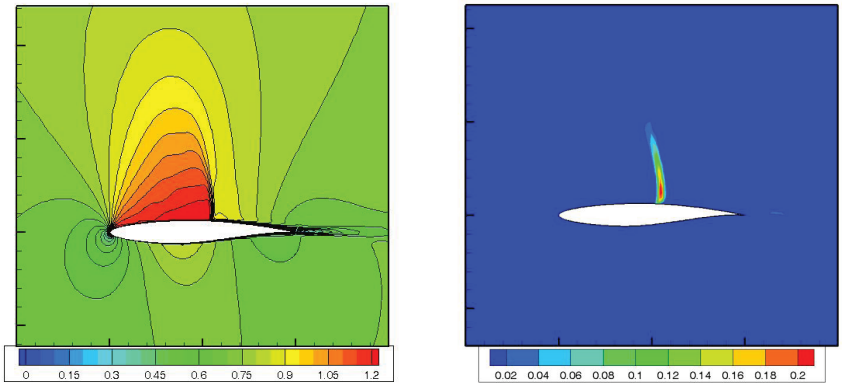
Figure 6: Density contours of the double Mach reflection. (a) Present; (b) Woodward and Colella [25].



(a) (b)

Figure 7: Pressure contours of the double Mach reflection. (a) Present; (b) Woodward and Colella [25].

https://doi.org/10.4208/aamm.2015.m1071 Published online by Cambridge University Press



(a) (b)

Figure 8: Contours of Mach number (a) and switch function (b) around the RAE2822 airfoil.

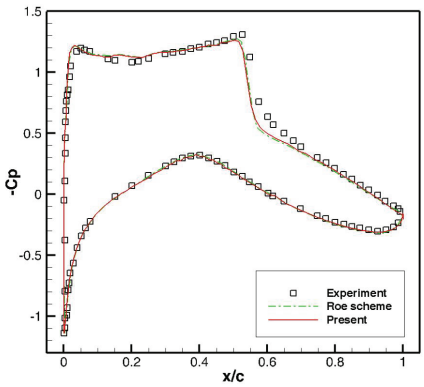


Figure 9: Comparison of pressure distribution on the RAE2822 airfoil surface.

type grid is adopted in this test case. To take turbulent effects [27–29] into consideration, the Spalart-Allmaras turbulent model is applied. Fig. 8 shows the Mach number contour obtained by present scheme and the switch function contour around airfoil. It can be seen from the figure that the switch function supplies sufficient dissipation around the strong shock waves and approaches to 0 in the smooth region, which matches well with the theory. The pressure coefficient distribution along the airfoil surface obtained by present scheme is compared with the experimental data [26] and numerical results of Roe scheme [30] in Fig. 9. These two numerical results are close to each other and both of them match well with the experimental data [26].

Case 5: Hypersonic flow around a half of cylinder

To investigate the capability of present scheme for simulation of hypersonic flows with strong shock waves, the hypersonic flow around a half of cylinder is simulated. The

https://doi.org/10.4208/aamm.2015.m1071 Published online by Cambridge University Press

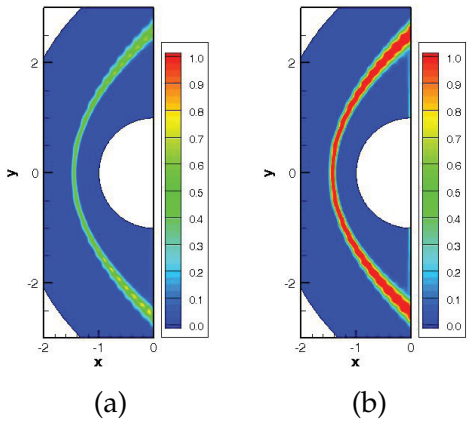


Figure 10: Contours of original switch function (a) and modified switch function (b) for hypersonic flow around a half of circular cylinder.

inflow condition of this case is [31]

$$M_\infty = 8.03, \quad Re = 1.835 \times 10^5, \quad T_\infty = 124.94K, \quad T_w = 294.44K.$$

In the current simulation, the computational mesh is 160×160, in which the cell Reynolds number is chosen as $Re_{cell} = \rho_\infty U_\infty \Delta r / \mu_\infty = 1.835$, where Δr is the mesh spacing of the first cell in the normal direction adjacent to the cylinder surface. To accelerate the convergence, the LU-SGS scheme [32] is applied to solve the governing equations.

At first, when the switch function is chosen as the way in Eq. (2.25), the heat flux exhibits oscillations in the vicinity of stagnation point. This is probably because the numerical dissipation introduced by the switch function in Eq. (2.25) is not sufficient in hypersonic flows. It can be verified with Fig. 10 that the switch function values did not approach 1 in the region around strong shock waves. In fact, the maximum value of the switch function is around 0.84. To overcome this deficiency, a minor revision is made to Eq. (2.25) for this hypersonic case. The new values of switch function are defined as

$$\eta^{++} = \max\{\eta_L^+, \eta_R^+\}, \tag{3.1}$$

where η_L^+ and η_R^+ are the maximum values of the switch function in the left and right control cells, respectively. Accordingly, the inviscid flux in Eq. (2.28) should be changed to

$$\mathbf{F}_c^* = (1-\eta^{++}) \cdot \mathbf{F}_{c,0}^* + \eta^{++} \cdot \mathbf{F}_{c,1}^*. \tag{3.2}$$

The contour of modified switch function is also displayed in Fig. 10. It is clear that the modified switch function values are larger than the original ones in the vicinity of strong shock waves.

The current results of pressure and temperature contours around the cylinder are presented in Fig. 11. It is clear that the "carbuncle phenomenon" and post-shock oscillations

https://doi.org/10.4208/aamm.2015.m1071 Published online by Cambridge University Press

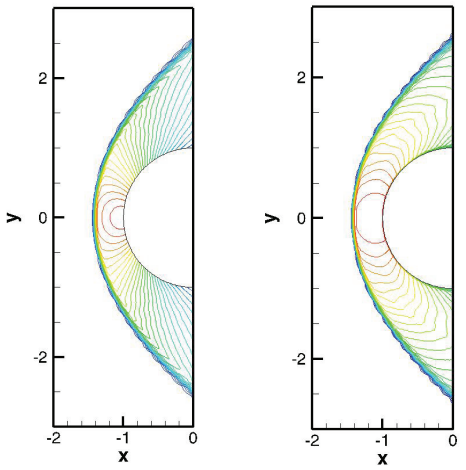


Figure 11: Pressure (a) and temperature (b) contours of hypersonic flow around a half of cylinder.

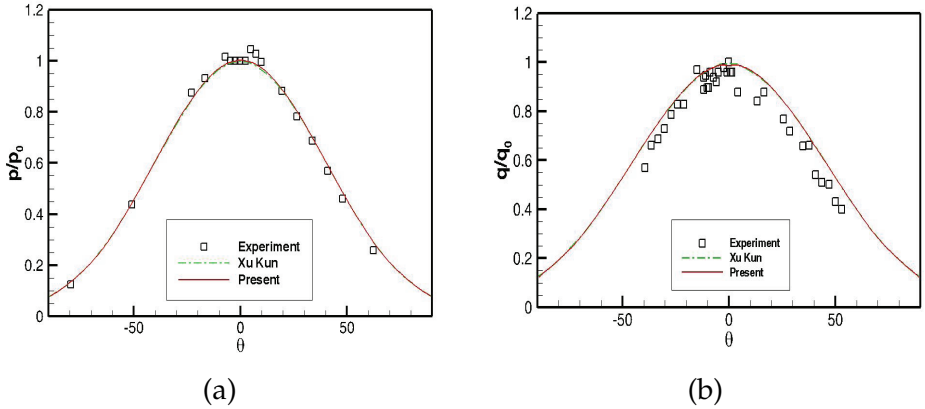


Figure 12: Pressure (a) and heat flux (b) distribution along the cylinderical surface.

are not appeared in the present results. Fig. 12 presents the normalized pressure and heat flux distribution along the half of cylinder surface, where the pressure p_0 is $p_0 = 0.9209$ and heat flux q_0 is $q_0 = 0.003655$. The experimental results [31] and numerical results of Xu [15] are also displayed in the figure for comparison. Good agreements can be found in Fig. 12, which verifies the capability of current SF-GKS in solving hypersonic flow problems.

4 Conclusions

In this work, a switch function-based gas-kinetic scheme (SF-GKS) is developed for simulation of compressible inviscid and viscous flows. The governing equations are dis-

https://doi.org/10.4208/aamm.2015.m1071 Published online by Cambridge University Press

cretized by the finite volume method and the present SF-GKS is applied to evaluate the convective flux across cell interface. Unlike the traditional gas-kinetic scheme in the calculation of inviscid flux such as Kinetic Flux Vector Splitting (KFVS), the numerical dissipation is controlled with a switch function in the present scheme. In this way, it is ensured that the numerical dissipation is only introduced in the region around strong shock waves. Another advantage is that the SF-GKS can be easily extended to viscous flow problems because the SF-GKS can well capture both strong shock waves and thin boundary layers simultaneously.

Several numerical simulations are performed to examine the capability of the proposed SF-GKS. At first, the inviscid compressible flows are tested, including 1-D Euler shock tube, regular shock reflection and double Mach reflection. Furthermore, the SF-GKS is extended to solve viscous compressible flow problems, such as the turbulent flow around RAE2822 airfoil and hypersonic flow around a half of cylinder. Numerical results are compared with the theoretical, experimental and/or numerical results in the literature. Good agreement in the comparisons well verifies the accuracy and robustness of present scheme.

References

[1] G. May, B. Srinivasan and A. Jameson, *An improved gas-kinetic BGK finite-volume method for three-dimensional transonic flow,* J. Comput. Phys., 220 (2007), pp. 856–878.
[2] D. Pullin, *Direct simulation methods for compressible inviscid ideal-gas flow,* J. Comput. Phys., 34 (1980), pp. 231–244.
[3] J. Mandal and S. Deshpande, *Kinetic flux vector splitting for Euler equations,* Comput. Fluids, 23 (1994), pp. 447–478.
[4] S. Y. Chou and D. Baganoff, *Kinetic flux-vector splitting for the Navier-Stokes equations,* J. Comput. Phys., 130 (1997), pp. 217–230.
[5] L. Yang, C. Shu and J. Wu, *A simple distribution function-based gas-kinetic scheme for simulation of viscous incompressible and compressible flows,* J. Comput. Phys., 274 (2014), pp. 611–632.
[6] K. Xu, *Gas-kinetic schemes for the unsteady compressible flow simulations,* VKI for Fluid Dynamics Lecture Series, (1998), 1998-03.
[7] K. Xu, Numerical Hydrodynamics from Gas-Kinetic Theory, Ph.D. Thesis, Columbia University, New York, 1993.
[8] K. H. Prendergast and K. Xu, *Numerical hydrodynamics from gas-kinetic theory,* J. Comput. Phys., 109 (1993), pp. 53–66.
[9] D. Chae, C. Kim and O.-H. Rho, *Development of an improved gas-kinetic BGK scheme for inviscid and viscous flows,* J. Comput. Phys., 158 (2000), pp. 1–27.
[10] K. Xu, *A gas-kinetic BGK scheme for the Navier-Stokes equations and its connection with artificial dissipation and Godunov method,* J. Comput. Phys., 171 (2001), pp. 289–335.
[11] P. L. Bhatnagar, E. P. Gross and M. Krook, *A model for collision processes in gases I. small amplitude processes in charged and neutral one-component systems,* Phys. Review, 94 (1954), 511.
[12] M. Su, K. Xu and M. Ghidaoui, *Low-speed flow simulation by the gas-kinetic scheme*, J. Comput. Phys., 150 (1999), pp. 17–39.

https://doi.org/10.4208/aamm.2015.m1071 Published online by Cambridge University Press

[13] S. JIANG AND G. NI, *A γ-model BGK scheme for compressible multifluids,* Int. J. Numer. Methods Fluids, 46 (2004), pp. 163–182.
[14] Z.-H. LI AND H.-X. ZHANG, *Study on gas kinetic unified algorithm for flows from rarefied transition to continuum,* J. Comput. Phys., 193 (2004), pp. 708–738.
[15] K. XU, M. MAO AND L. TANG, *A multidimensional gas-kinetic BGK scheme for hypersonic viscous flow,* J. Comput. Phys., 203 (2005), pp. 405–421.
[16] Z. GUO, H. LIU, L.-S. LUO AND K. XU, *A comparative study of the LBE and GKS methods for 2D near incompressible laminar flows,* J. Comput. Phys., 227 (2008), pp. 4955–4976.
[17] J. JIANG AND Y. QIAN, *Implicit gas-kinetic BGK scheme with multigrid for 3D stationary transonic high-Reynolds number flows,* Comput. Fluids, 66 (2012), pp. 21–28.
[18] L. YANG, C. SHU, J. WU, N. ZHAO AND Z. LU, *Circular function-based gas-kinetic scheme for simulation of inviscid compressible flows,* J. Comput. Phys., 255 (2013), pp. 540–557.
[19] W. LI, M. KANEDA AND K. SUGA, *An implicit gas kinetic BGK scheme for high temperature equilibrium gas flows on unstructured meshes,* Comput. Fluids, 93 (2014), pp. 100–106.
[20] S. LIU, P. YU, K. XU AND C. ZHONG, *Unified gas-kinetic scheme for diatomic molecular simulations in all flow regimes,* J. Comput. Phys., 259 (2014), pp. 96–113.
[21] V. VENKATAKRISHNAN, *Convergence to steady state solutions of the Euler equations on unstructured grids with limiters,* J. Comput. Phys., 118 (1995), pp. 120–130.
[22] B. VAN LEER, *Towards the ultimate conservative difference scheme IV. A new approach to numerical convection,* J. Comput. Phys., 23 (1977), pp. 276–299.
[23] E. F. TORO, Riemann Solvers and Numerical Methods for Fluid Dynamics: a Practical Introduction, Springer Science & Business Media, 2009.
[24] MITTAL, SANJAY AND T. TEZDUYAR, *A unified finite element formulation for compressible and incompressible flows using augmented conservation variables*, Comput. Methods Appl. Mech. Eng., 161 (1998), pp. 229–243.
[25] P. WOODWARD AND P. COLELLA, *The numerical simulation of two-dimensional fluid flow with strong shocks*, J. Comput. Phys., 54 (1984), pp. 115–173.
[26] P. H. COOK, M. A. MCDONALD AND M. C. P. FIRMIN, *Aerofoil RAE2822-pressure distributions, and boundary layer and wake measurements,* AGARD Report AR 138, (1979).
[27] C. B. LEE AND S. WANG, *Study of the shock motion in a hypersonic shock system/turbulent boundary layer interaction,* Exp. Fluids, 19 (1995), pp. 143–149.
[28] C. B. LEE, Z. X. HONG, Y. S. KACHANOV, V. I. BORODULIN AND V. V. GAPONENKO, *A study in transitional flat plate boundary layers: measurement and visualization,* Exp. Fluids, 28 (2000), pp. 243–251.
[29] C. B. LEE AND J. Z. WU, *Transition in wall-bounded flows,* Appl. Mech. Rev., 61 (2008), 0802.
[30] K. KIM, C. KIM, O. H. RHO AND S. HONG, *Cure for shock instability: development of an improved Roe scheme,* AIAA Paper, 548 (2002), 2002.
[31] A. WIETING AND M. HOLDEN, *Experimental study of shock wave interference heating on a cylinder leading edge,* AIAA Paper, (1988).
[32] S. YOON AND A. JAMESON, *Lower-upper symmetric-Gauss-Seidel method for the Euler and Navier-Stokes equations,* AIAA J., 26 (1988), pp. 1025–1026.

https://doi.org/10.4208/aamm.2015.m1071 Published online by Cambridge University Press